

Field-Free Superconducting Diode Enabled by Geometric Asymmetry and Perpendicular Magnetization

Jiaxu Li, Zijian Zhang, Shiqi Wang, Yu He, Haochang Lyu, Qiusha Wang, Bowen Dong, Daoqian Zhu, Hisakazu Matsuki, Dapeng Zhu, Guang Yang, Weisheng Zhao*

J. X. Li, Z. J. Zhang, S. Q. Wang, Y. He, Q. S. Wang, D. Q. Zhu, G. Yang, W. S. Zhao
School of Integrated Circuit Science and Engineering, Beihang University, Beijing 100191, China
E-mail: gy251@buaa.edu.cn

H. C. Lyu, B. W. Dong
Beijing Superstring Academy of Memory Technology, Beijing 100176, China

Hisakazu Matsuki
Toyota Riken-Kyoto University Research Center (TRiKUC), Kyoto 606-8501, Japan

D. P. Zhu, G. Yang
Integrated Circuit and Intelligent Instruments Innovation Center, Qingdao Research Institute, Beihang University, Qingdao 266100, China

Keywords: superconducting diode effect; perpendicular magnetic anisotropy; ferromagnet/superconductor heterostructures

The superconducting diode effect (SDE)—manifested as directional, dissipationless supercurrents—is pivotal for realizing energy-efficient superconducting logic and memory technologies. Achieving high-efficiency SDE without external magnetic fields, however, remains a fundamental challenge. Here, we report a strongly enhanced, field-free SDE in Pt/Co/Nb heterostructures, enabled by the interplay of engineered geometric asymmetry and stray fields from a perpendicularly magnetized Co layer. This configuration promotes directional vortex entry and spatially selective pinning, yielding diode efficiencies that exceed all previously reported field-free values. Temperature- and field-dependent transport measurements, supported by micromagnetic simulations, reveal that the enhanced nonreciprocity stems from three cooperative mechanisms: asymmetric vortex entry, localized magnetic pinning, and Lorentz-force imbalance. These findings establish a scalable, CMOS-compatible platform for high-performance superconducting rectifiers, offering new opportunities for cryogenic spintronics and quantum electronics.

1. Introduction

The superconducting diode effect (SDE)^[1–6], characterized by nonreciprocal critical currents, enables dissipationless supercurrent in one direction while exhibiting finite resistance in the opposite direction. This nonreciprocal behavior holds great promise for energy-efficient superconducting rectification, quantum circuits, and scalable superconducting computing systems^[7–10]. Fundamentally, the realization of SDE requires the simultaneously breaking of time-reversal symmetry (TRS) and spatial inversion symmetry (SIS). TRS is typically broken via external magnetic fields^[11,12], induced proximity magnetism from ferromagnetic layers^[10,13,14], or by trapping Abrikosov vortices^[15,16]. SIS breaking, on the other hand, is commonly achieved through structural asymmetry, including device-level geometry^[4,7,10,17], intrinsic crystallography^[1,18], or localized defects^[19,20].

In type-II superconductors, vortex dynamics play a central role in determining the onset of dissipation. Magnetic flux penetrates the material as quantized vortices, and their motion under current induces resistive losses. Controlling vortex motion through geometric or magnetic inhomogeneities is thus essential to preserve superconductivity. Previous studies have demonstrated enhanced nonreciprocal transport by engineering asymmetric vortex pinning landscapes^[4,7,10,17,21], while stray fields from adjacent ferromagnetic layers offer a means to break TRS and control vortex entry without external fields^[10,13,22].

Despite these advances, a unified understanding of how spatially graded stray fields shape vortex dynamics—and their role in boosting field-free SDE efficiency—remains lacking. In particular, the effect of local stray field gradients (rather than uniform field magnitude) on vortex entry, pinning, and depinning has not been systematically explored. Moreover, achieving high-efficiency, field-free diode functionality in scalable, CMOS-compatible systems remains a critical challenge.

In this work, we address these issues by designing ferromagnet/superconductor (FM/SC) heterostructures that combine engineered geometric asymmetry with perpendicular magnetic anisotropy (PMA). The triangular geometry introduces directional asymmetry in vortex entry barriers, while the PMA-Co layer generates strong, spatially graded out-of-plane stray fields (B_z) that act as both pinning and depinning modulators. Through detailed experiments and micromagnetic simulations, we identify three cooperative mechanisms that underpin the observed high-efficiency SDE: (i) preferential vortex entry on the symmetric side, (ii) enhanced vortex pinning on the asymmetric side due to localized magnetic wells, and (iii) Lorentz-force asymmetry that favors vortex depinning under reverse bias. Our approach enables the highest reported field-free superconducting diode efficiency while maintaining full CMOS

compatibility. These results demonstrate the key role of spatially graded B_z fields and establish PMA-Co-based heterostructures as a robust, scalable platform for high-performance cryogenic logic and memory applications.

2. Results and Discussions

All samples were fabricated on thermally oxidized silicon substrates using DC magnetron sputtering in an ultrahigh vacuum system with a base pressure below 10^{-8} Torr at room temperature. The multilayer stack was composed of substrate//Ta(2 nm)/Pt(3 nm)/Co(0.9 nm)/Nb(40 nm). This configuration was selected to ensure robust PMA (see Supplementary Note S1) while preserving continuous superconducting properties. Device patterning was carried out using electron-beam lithography (EBL) with a positive photoresist, followed by electron-beam evaporation of a 120 nm-thick Al layer, which served as a hard mask. After standard lift-off in acetone, the Al mask was used for pattern transfer via ion beam etching (IBE). Residual Al was subsequently removed using tetramethylammonium hydroxide (TMAH).

Two types of device geometries were fabricated:

- **Sample 1 (asymmetric geometry):** A superconducting strip with a triangular protrusion on one side to intentionally break structural inversion symmetry. The strip measured $100\ \mu\text{m}$ in length and $5\ \mu\text{m}$ in width, with the protrusion having a base of $10\ \mu\text{m}$ and a height of $3.5\ \mu\text{m}$.
- **Sample 2 (symmetric geometry):** A reference Hall bar device of identical dimensions but without any geometric asymmetry.

Figure 1a presents a scanning electron micrograph (SEM) of the asymmetric device alongside a schematic illustrating its operating principle. Figure 1b shows the R - T characteristics of both symmetric and asymmetric devices. Both sample exhibit sharp superconducting transitions, with the symmetric device displaying a slightly higher critical temperature ($T_c = 6.5\ \text{K}$) than its asymmetric counterpart ($T_c = 6.3\ \text{K}$). This small difference likely results from local strain or edge perturbations introduced by the protrusion, which may slightly suppress superconductivity at the edge without compromising overall film uniformity.

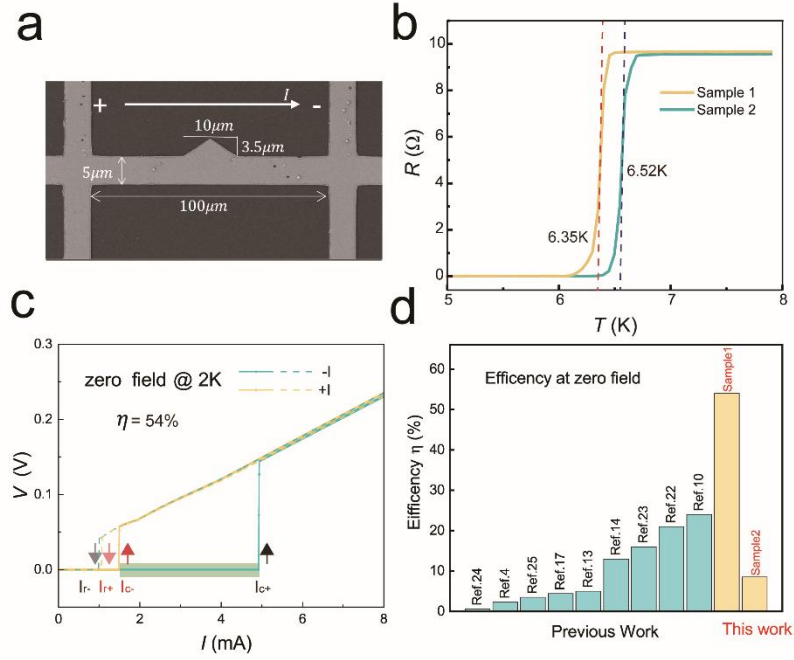


Figure 1. Device geometry and transport behavior of symmetric and asymmetric superconducting diodes. (a) Scanning electron micrograph of the asymmetric device (Sample 1), showing a triangular protrusion on the upper edge. The main strip is 100 μm long and 5 μm wide; the protrusion has a base of 10 μm and a height of 3.5 μm . The white arrow indicates the direction of current flow. (b) R - T curves of symmetric and asymmetric devices measured from 5 K to 8 K under a constant current of 100 μA , showing sharp superconducting transitions and a small difference in T_c . (c) I - V characteristics of the asymmetric device at 2 K under zero magnetic field. Arrows indicate the direction of voltage response under forward and reverse bias. (d) Comparison of field-free superconducting diode efficiency η between our devices and previously reported results across various material systems and device configurations.

Figure 1c shows the I - V characteristics of the asymmetric device (Sample 1) measured at 2 K under zero magnetic field. The positive critical current (I_c^+) reaches 4.92 mA, while the negative critical current (I_c^-) is 1.48 mA, yielding a diode efficiency of $\eta = \frac{I_c^+ - |I_c^-|}{I_c^+ + |I_c^-|} = 54\%$. This value significantly exceeds previously reported results for comparable FM/SC systems^[13,14,20]. Figure 1d compares the diode efficiency of the asymmetric device (Sample 1) and the symmetric control device (Sample 2) with a broad range of previously reported values across various material systems and structural configurations^[4,10,13,14,17,22–25]. Notably, Sample 1 achieves the highest field-free diode efficiency reported to date, demonstrating the strong synergy between geometric asymmetry and perpendicular magnetization. In contrast, the symmetric reference device shows substantially lower efficiency under identical zero-field conditions, emphasizing the crucial role of inversion symmetry breaking. The enhanced

nonreciprocity originates from asymmetric vortex dynamics induced by the triangular protrusion, which modifies local surface barriers and promotes current crowding. In addition, the perpendicularly magnetized Co layer generates intrinsic stray fields that distort the Meissner state and facilitate vortex penetration. This combined geometric and magnetic asymmetry amplifies directional vortex motion, establishing the foundation for the highly efficient field-free SDE observed in our devices.

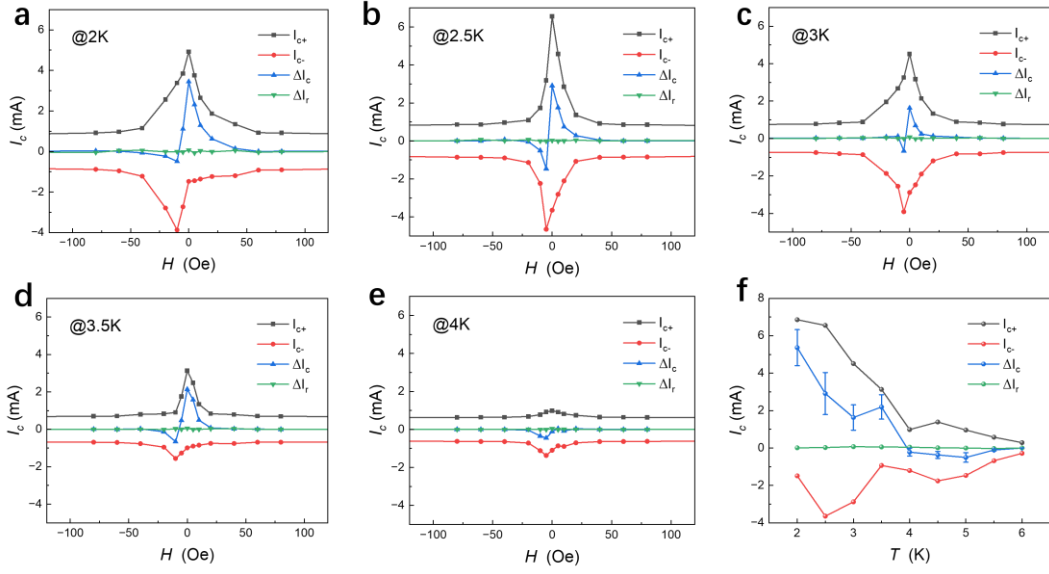


Figure 2. Magnetic field and temperature dependence of the superconducting diode effect in the asymmetric device. (a)-(e) Evolution of critical currents I_c^+ and I_c^- in the asymmetric device (Sample 1) under various out-of-plane magnetic fields at temperatures of 2 K, 2.5 K, 3 K, 3.5 K, and 4 K, respectively. (f) Temperature dependence of the nonreciprocal component $\Delta I_c = I_c^+ - |I_c^-|$ at zero magnetic field, showing a monotonic decrease with increasing temperature and vanishing near T_c , consistent with thermal suppression of vortex asymmetry.

Vortex behavior in type-II superconductors is highly sensitive to temperature. Thermal fluctuations affect vortex pinning strength, mobility, and annihilation dynamics, all of which influence the stability of nonreciprocal transport.^[26–28] To investigate this, we systematically measured the nonreciprocal current component, defined as $\Delta I_c = I_c^+ - |I_c^-|$, over a temperature range of 2 K to 4 K, as shown in Figures 2a-e. Field-dependent I - V characteristics of Sample 1 at 2 K are provided in Supplementary Note S2. Notably, the nonreciprocal critical current is maximized at zero magnetic field, even after reversing the magnetization direction of the Co layer (Supplementary Note S3), indicating that stray field-induced vortex asymmetry is most prominent in the absence of external fields. Introducing an external magnetic field disrupts this balance, gradually restoring symmetry in vortex dynamics and thereby reducing the diode efficiency. Figure 2f summarizes the temperature dependence of ΔI_c at zero magnetic field. A

clear monotonic decrease is observed with increasing temperature, and ΔI_c vanishes near T_c , further confirming the key role of vortex dynamics in determining SDE efficiency.

At low temperatures, the superconducting state is robust, vortex density remains low, and vortex-vortex interactions are weak. In this regime, local factors—such as stray fields, structural inhomogeneity, or geometric asymmetry—dominate vortex motion, resulting in strong directionality and pronounced nonreciprocity. As temperature increases, the superconducting gap narrows and vortex density rises, leading to enhanced vortex-vortex interactions that destabilize the asymmetric configuration^[29]. Simultaneously, the critical current decreases, and thermal activation becomes more prominent. Thermally assisted vortex depinning and hopping reduce the effectiveness of pinning centers and increase vortex mobility, further diminishing the diode effect. Previous studies have shown that vortex matter undergoes a crossover from a quasi-solid phase (e.g., vortex glass or Bragg glass) to a more fluid-like state at higher temperatures^[27,30–33]. In this high-temperature regime, thermal fluctuations weaken vortex pinning and erode the geometric control over vortex trajectories, ultimately suppressing the efficiency of nonreciprocal transport.

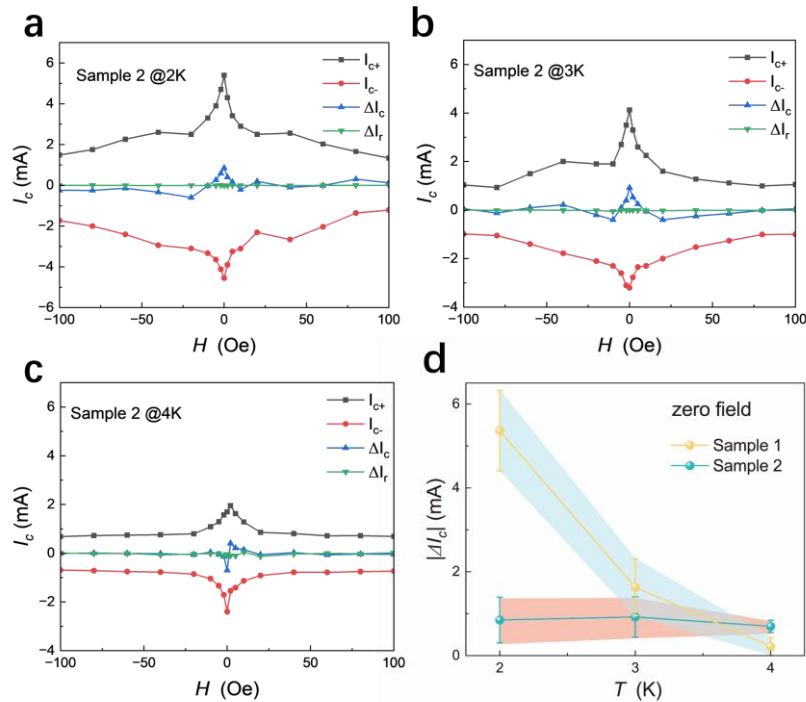


Figure 3. Comparison of critical current behavior in symmetric and asymmetric superconducting devices. (a)-(c) Magnetic field dependence of the critical currents I_c^+ and I_c^- for the symmetric device (Sample 2) at 2 K, 3 K, and 4 K, respectively, showing minimal nonreciprocity across all temperatures and field conditions. (d) Comparison of the nonreciprocal current component ΔI_c under zero magnetic field for the asymmetric (Sample 1) and symmetric (Sample 2) devices at various temperatures. Colored bands represent error margins based on repeated measurements, reflecting experimental uncertainty.

We compared the I - V characteristics of the symmetric device (Sample 2) at 2 K, 3 K, and 4 K, as shown in Figures 3a-c. While a weak diode effect is observable at all temperatures, its magnitude is significantly lower than that of the asymmetric structure. Figure 3d directly compares ΔI_c between the two devices. The asymmetric structure exhibits a much larger ΔI_c , particularly at low temperatures. At 2 K, ΔI_c reaches 5.4 mA in the asymmetric sample—over six times higher than the 0.85 mA measured in the symmetric counterpart. This substantial enhancement arises from the directional modulation of vortex dynamics enabled by the engineered geometry. Specifically, the triangular protrusion in the asymmetric device modifies the local vortex entry barrier, promoting stronger pinning on one side while allowing easier vortex motion on the other. This anisotropic behavior results in pronounced nonreciprocal transport. In contrast, the symmetric device lacks features that break inversion symmetry, leading to a uniform vortex landscape and a significantly weaker SDE. These results highlight geometric asymmetry as a key parameter for controlling vortex behavior, particularly in the low-temperature regime where thermal fluctuations are minimal.

In type-II superconductors, vortex dynamics are governed by the interplay between Lorentz forces and pinning forces. In the absence of an external magnetic field, Lorentz forces arise from the interaction between the current and stray fields generated by the adjacent ferromagnetic layer. When the ferromagnet exhibits uniform perpendicular magnetization, it produces out-of-plane stray fields that penetrate the superconducting layer. In asymmetric structures, this field distribution becomes highly inhomogeneous, inducing asymmetric Meissner screening currents along the device edges^[34]. Recent studies have identified such asymmetric screening currents as essential for achieving the SDE, especially in systems with broken inversion symmetry^[22].

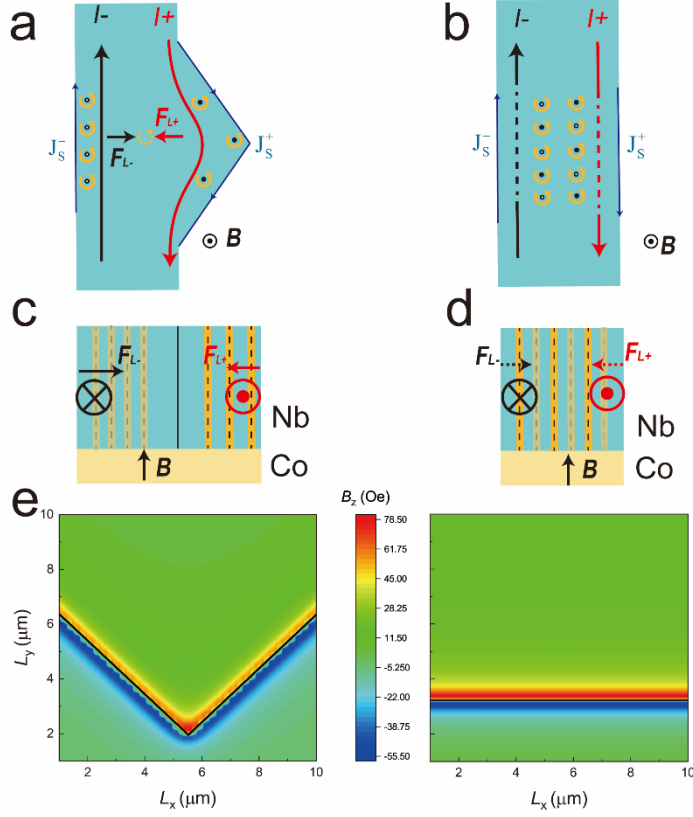


Figure 4. Vortex dynamics and stray field distribution in asymmetric and symmetric superconducting devices. (a) and (c) correspond to the asymmetric device. (a) Schematic top view illustrating vortex trajectories under forward and reverse current bias. Vortices are represented as ring-like structures with central dots, and blue arrows indicate Meissner screening currents. The triangular protrusion induces directional asymmetry in vortex entry. (c) Cross-sectional views under positive and negative bias, respectively. Light and dark yellow stripes denote the vortex pinning potential, and the black dashed line marks the location of the pinning center. (b) and (d) correspond to the symmetric device. (b) Schematic top view of the structure without geometric asymmetry. (d) Cross-sectional views under positive and negative bias, illustrating symmetric vortex behavior due to the uniform geometry. (e) Contour map of the local stray field distribution near the asymmetric and symmetric edge regions, highlighting the spatial variation introduced by geometric asymmetry.

Figure 4 provides a comprehensive illustration of vortex dynamics and stray field distributions in asymmetric and symmetric superconducting devices. Figure 4a shows how the triangular protrusion increases the local vortex entry barrier on the asymmetric side, thereby modulating the vortex potential landscape. This geometric asymmetry induces spatially nonuniform stray fields near the device edges, denoted as $B_{stray}^{A/S}$ for the asymmetric and symmetric sides, respectively. As shown in the MuMax3-simulated contour maps in Figure 4e, the average stray field magnitude on the asymmetric side (B_{stray}^A) is lower than that on the symmetric side (B_{stray}^S). In the absence of a bias current, the local Meissner screening currents

at the asymmetric and symmetric edges can be expressed as $J_s^+ = \alpha B_{stray}^A$ and $J_s^- = \alpha B_{stray}^S$, respectively, where α is a proportionality constant^[22]. The weaker screening current on the asymmetric side leads to a higher surface barrier for vortex entry, thus suppressing vortex penetration from that edge^[12,35]. As a result, vortices preferentially enter from the symmetric side.

Micromagnetic simulations further reveal a steeper spatial gradient of the stray field near the asymmetric edge. This gradient gives rise to localized magnetic potential wells, which serves as strong pinning centers for the fewer vortices that manage to enter this region^[36–38], as schematically illustrated in Figure 4c. These two effects—preferential vortex entry at the symmetric side and enhanced pinning at the asymmetric side—cooperatively produce a spatially asymmetric distribution of vortex dynamics and dissipation. Together, they constitute the first two synergistic mechanisms underpinning the SDE.

We now turn to the dynamic behavior under an applied current J_{ext} to examine a third cooperative mechanism governing the nonreciprocal response. Under current bias, the total current density in the superconducting layer is given by $J_{tot} = J_{ext} + J_s^\pm$. The Lorentz force acting on edge-localized vortices is given by $F_L = J_{tot} \times B_z$, where B_z denotes the out-of-plane stray field produced by the Co layer. Under forward bias (I^+), this Lorentz force acts predominantly on the asymmetric edge and is given by $F_{L+} = (J_{ext} + \alpha B_{stray}^A) \times \phi_0$, where ϕ_0 is the magnetic flux quantum^[17,20]. Under reverse bias (I^-), the Lorentz force acts mainly on the symmetric edge, yielding $F_{L-} = (J_{ext} + \alpha B_{stray}^S) \times \phi_0$. Since $B_{stray}^A < B_{stray}^S$, it follows that $F_{L+} < F_{L-}$. This asymmetry in Lorentz force implies that vortices on the asymmetric edge experience a weaker driving force under forward bias, making them less likely to be depinned from strong pinning centers. In contrast, under reverse bias, the stronger Lorentz force is more effective at overcoming the weaker pinning at the symmetric edge, resulting in earlier dissipation. Consequently, a higher critical current I_c^+ is required to initiate vortex motion under forward bias, while a lower critical current I_c^- suffices under reverse bias. This Lorentz-force asymmetry constitutes a third cooperative mechanism, which—together with asymmetric entry barriers and spatially selective pinning—accounts for the high-efficiency SDE observed in our devices. By contrast, Figures 4b and 4d show that the symmetric reference device lacks geometric asymmetry, resulting in balanced vortex entry, uniform pinning, and negligible directional variation in Lorentz force—consistent with its nearly reciprocal transport behavior.

To further elucidate the microscopic origin of the spatially graded stray fields discussed above, we performed micromagnetic simulations comparing devices with PMA and in-plane

magnetic anisotropy (IMA), as shown in Figure 5. These simulations reveal how the interplay between device geometry and magnetic anisotropy governs the formation of stray-field gradients, and highlight the essential role of PMA in enabling nonreciprocal vortex dynamics and the superconducting diode effect.

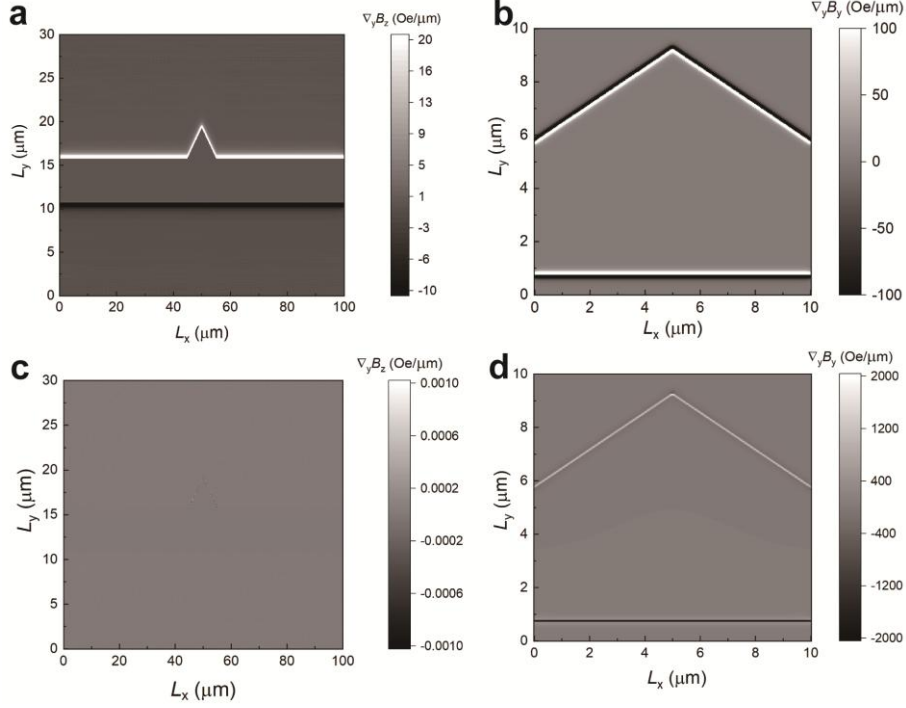


Figure 5. Micromagnetic simulations of stray field gradients in asymmetric devices with PMA and IMA. (a) Simulated spatial gradient of the out-of-plane stray field component B_z along the y -direction at the upper and lower edges of the PMA-Co device, showing enhanced variation near the triangular protrusion. (b) Simulated gradient of the in-plane stray field component B_y at a height of 40 nm above the Co layer, corresponding to the Nb surface. (c, d) Corresponding B_z and B_y gradient profiles for an identical geometry with IMA-Co, showing negligible B_z gradients and similar B_y behavior to the PMA case. These results highlight the essential role of spatially graded out-of-plane fields in enabling the SDE.

Figures 5a and 5b present the simulated stray-field gradients in the PMA configuration. The out-of-plane magnetized Co layer generates substantial B_z components with steep spatial gradients, particularly near the geometric transition between the rectangular and triangular regions. Figure 5a shows the gradient of B_z along the y -direction at the device edges (simulated over a $100 \mu\text{m} \times 30 \mu\text{m} \times 1 \text{ nm}$ region), while Figure 5b shows the corresponding B_y gradient at 40 nm above the Co layer (i.e., the Nb surface) within a $10 \mu\text{m} \times 10 \mu\text{m} \times 41 \text{ nm}$ domain. While minor modulation of B_y is observed, its spatial gradient is relatively weak and symmetric. These results confirm that in the asymmetric configuration, PMA not only enhances

the magnitude of B_z but also introduces steep and localized B_z gradient, both of which are critical for directional vortex control.

To isolate the role of magnetic anisotropy, we simulated an identical geometry with in-plane magnetization by increasing the Co thickness to 2 nm and setting the uniaxial anisotropy constant $K_u = 0$. zero. A 0.1 T external field was applied along the y-direction to uniformly align the magnetization. The IMA results (Figures 5c and 5d) exhibit negligible B_z gradients compared to the PMA case. Although minor inhomogeneities in B_y arise from magnetization nonuniformity, the lack of significant out-of-plane stray fields renders the IMA configuration ineffective for driving nonreciprocal vortex transport. These findings demonstrate that the presence of a spatially nonuniform out-of-plane stray field—not merely its magnitude—is crucial for inducing nonreciprocal vortex dynamics. Compared to the IMA configuration, PMA-Co heterostructures produce stronger B_z fields and steeper spatial gradients at the device edges—conditions essential for realizing efficient, field-free superconducting diode operation.

Notably, our PMA-Co approach differs from previous reports on EuS-based ferromagnetic insulators, where sizable B_z fields arise from intrinsic $4f$ orbital moments—even under in-plane magnetization^[39,40]. Although those systems can support SDE, their reliance on material-specific magnetic properties limits scalability and integration. In contrast, our PMA-based design achieves the highest field-free superconducting diode efficiency reported to date, while utilizing a fully CMOS-compatible and fabrication-friendly material platform. These combined advantages establish PMA-Co heterostructures as a robust and scalable foundation for integrating high-performance superconducting diodes into next-generation cryogenic spintronic, logic, and memory architectures^[41].

3. Conclusion

In summary, we have demonstrated that combining geometric asymmetry with stray fields from a perpendicularly magnetized ferromagnetic layer enables efficient modulation of vortex dynamics, leading to a strongly enhanced SDE under zero external magnetic field. By engineering asymmetric FM/SC heterostructures, we establish a clear microscopic link between spatial stray-field gradients, directional vortex pinning, and nonreciprocal superconducting transport. These results provide direct insight into the mechanism of field-free SDE and suggest that further enhancements may be achieved through magnetization control or advanced structural design. The robust, geometry-driven SDE presented here offers a scalable, CMOS-compatible approach to superconducting device engineering, with strong potential for low-power, non-volatile logic and memory applications in cryogenic and quantum technologies.

References

- [1] F. Ando, Y. Miyasaka, T. Li, J. Ishizuka, T. Arakawa, Y. Shiota, T. Moriyama, Y. Yanase, T. Ono, *Nature* **2020**, *584*, 373.
- [2] A. Daido, Y. Ikeda, Y. Yanase, *Phys. Rev. Lett.* **2022**, *128*, 037001.
- [3] M. Nadeem, M. S. Fuhrer, X. Wang, *Nat. Rev. Phys.* **2023**, *5*, 558.
- [4] X. Zhang, Q. Huan, R. Ma, X. Zhang, J. Huang, X. Liu, W. Peng, H. Li, Z. Wang, X. Xie, L. You, *Adv. Quantum Technol.* **2024**, *7*, 2300378.
- [5] H. F. Legg, D. Loss, J. Klinovaja, *Phys. Rev. B* **2022**, *106*, 104501.
- [6] C. Li, Y.-Y. Lyu, W.-C. Yue, P. Huang, H. Li, T. Li, C.-G. Wang, Z. Yuan, Y. Dong, X. Ma, X. Tu, T. Tao, S. Dong, L. He, X. Jia, G. Sun, L. Kang, H. Wang, F. M. Peeters, M. V. Milošević, P. Wu, Y.-L. Wang, *Nano Lett.* **2024**, *24*, 4108.
- [7] M. Castellani, O. Medeiros, A. Buzzi, R. A. Foster, M. Colangelo, K. K. Berggren, *Nat. Electron.* **2025**, *8*, 417.
- [8] *Nat. Electron.* **2025**, *8*, 375.
- [9] D. Kochan, C. Strunk, *Nat. Electron.* **2025**, *8*, 380.
- [10] J. Ingla-Aynés, Y. Hou, S. Wang, E.-D. Chu, O. A. Mukhanov, P. Wei, J. S. Moodera, *Nat. Electron.* **2025**, *8*, 411.
- [11] A. Daido, Y. Yanase, *Phys. Rev. B* **2022**, *106*, 205206.
- [12] D. Suri, A. Kamra, T. N. G. Meier, M. Kronseder, W. Belzig, C. H. Back, C. Strunk, *Appl. Phys. Lett.* **2022**, *121*, 102601.
- [13] Y. Cheng, Q. Shu, H. He, B. Dai, K. L. Wang, *Adv. Mater.* **2025**, 2415480.
- [14] J. Xiong, J. Xie, B. Cheng, Y. Dai, X. Cui, L. Wang, Z. Liu, J. Zhou, N. Wang, X. Xu, X. Chen, S.-W. Cheong, S.-J. Liang, F. Miao, *Nat. Commun.* **2024**, *15*, 4953.
- [15] B. L. T. Plourde, D. J. Van Harlingen, D. Yu. Vodolazov, R. Besseling, M. B. S. Hesselberth, P. H. Kes, *Phys. Rev. B* **2001**, *64*, 014503.
- [16] D. Y. Vodolazov, F. M. Peeters, *Phys. Rev. B* **2005**, *72*, 172508.
- [17] Y. He, Z. Wang, J. Li, F. Zhong, H. Yang, K. Shi, L. Wang, G. Yang, W. Zhao, *Adv. Funct. Mater.* **2025**, 2505766.
- [18] M. S. Anwar, T. Nakamura, R. Ishiguro, S. Arif, J. W. A. Robinson, S. Yonezawa, M. Sigrist, Y. Maeno, *Commun. Phys.* **2023**, *6*, 290.
- [19] N. Satchell, P. M. Shepley, M. Algarni, M. Vaughan, E. Darwin, M. Ali, M. C. Rosamond, L. Chen, E. H. Linfield, B. J. Hickey, G. Burnell, *Appl. Phys. Lett.* **2020**, *116*, 022601.
- [20] Y. Hou, F. Nichele, H. Chi, A. Lodesani, Y. Wu, M. F. Ritter, D. Z. Haxell, M. Davydova, S. Ilić, O. Glezakou-Elbert, A. Varambally, F. S. Bergeret, A. Kamra, L. Fu, P. A. Lee, J. S. Moodera, *Phys. Rev. Lett.* **2023**, *131*, 027001.
- [21] H. H. Edwards, V. L. Newhouse, *J. Appl. Phys.* **1962**, *33*, 868.
- [22] Y. Hou, F. Nichele, H. Chi, A. Lodesani, Y. Wu, M. F. Ritter, D. Z. Haxell, M. Davydova, S. Ilić, O. Glezakou-Elbert, A. Varambally, F. S. Bergeret, A. Kamra, L. Fu, P. A. Lee, J. S. Moodera, *Phys. Rev. Lett.* **2023**, *131*, 027001.
- [23] K.-R. Jeon, J.-K. Kim, J. Yoon, J.-C. Jeon, H. Han, A. Cottet, T. Kontos, S. S. P. Parkin, *Nat. Mater.* **2022**, *21*, 1008.
- [24] N. Satchell, P. Shepley, M. Rosamond, G. Burnell, *J. Appl. Phys.* **2023**, *133*, 203901.
- [25] J. He, Y. Ding, X. Zeng, Y. Zhang, Y. Wang, P. Dong, X. Zhou, Y. Wu, K. Cao, K. Ran, J. Wang, Y. Chen, K. Watanabe, T. Taniguchi, S.-L. Yu, J.-X. Li, J. Wen, J. Li, **2024**, DOI 10.48550/arXiv.2409.04093.
- [26] M. Buchacek, R. Willa, V. B. Geshkenbein, G. Blatter, *Phys. Rev. B* **2019**, *100*, 014501.
- [27] G. W. Crabtree, D. R. Nelson, *Phys. Today* **1997**, *50*, 38.

- [28] D. Y. Vodolazov, F. M. Peeters, *Phys. Rev. B* **2007**, *76*, 014521.
- [29] D. Cerbu, V. N. Gladilin, J. Cuppens, J. Fritzsche, J. Tempere, J. T. Devreese, V. V. Moshchalkov, A. V. Silhanek, J. Van de Vondel, *New J. Phys.* **2013**, *15*, 063022.
- [30] G. Blatter, *Rev. Mod. Phys.* **1994**, *66*, 1125.
- [31] T. Nattermann, S. and Scheidl, *Adv. Phys.* **2000**, *49*, 607.
- [32] M. S. Li, T. Nattermann, *Phys. Rev. B* **2003**, *67*, 184520.
- [33] E. Zhang, X. Xu, Y.-C. Zou, L. Ai, X. Dong, C. Huang, P. Leng, S. Liu, Y. Zhang, Z. Jia, X. Peng, M. Zhao, Y. Yang, Z. Li, H. Guo, S. J. Haigh, N. Nagaosa, J. Shen, F. Xiu, *Nat. Commun.* **2020**, *11*, 5634.
- [34] D. Y. Vodolazov, F. M. Peeters, I. V. Grigorieva, A. K. Geim, *Phys. Rev. B* **2005**, *72*, 024537.
- [35] A. Gurevich, *AIP Adv.* **2015**, *5*, 017112.
- [36] G. Blatter, M. V. Feigel'man, V. B. Geshkenbein, A. I. Larkin, V. M. Vinokur, *Rev. Mod. Phys.* **1994**, *66*, 1125.
- [37] V. R. Misko, S. Savel'ev, A. L. Rakhmanov, F. Nori, *Phys. Rev. B* **2007**, *75*, 024509.
- [38] G. Blatter, M. V. Feigel'man, V. B. Geshkenbein, A. I. Larkin, V. M. Vinokur, *Rev. Mod. Phys.* **1994**, *66*, 1125.
- [39] J. Rhyne, T. McGuire, *IEEE Trans. Magn.* **1972**, *8*, 105.
- [40] H. R. Kirchmayr, C. A. Poldy, *J. Magn. Magn. Mater.* **1978**, *8*, 1.
- [41] J. A. Kittl, A. Lauwers, O. Chamirian, M. Van Dal, A. Akheyar, M. De Potter, R. Lindsay, K. Maex, *Microelectron. Eng.* **2003**, *70*, 158.

Supplementary Note S1. Magnet characterization of the Co layer.

To verify the magnetic properties of the Co layer, vibrating sample magnetometry (VSM) measurements were performed at room temperature, as shown in Figure S1. The hysteresis loop reveals a clear magnetic response, indicating strong perpendicular magnetic anisotropy, consistent with previous reports on ultrathin Co films^[1,2].

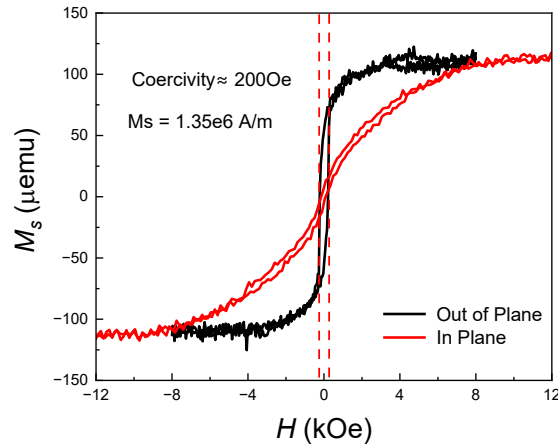


Figure S1. Magnetic hysteresis loop of the Co layer measured at room temperature.

Supplementary Note S2. Field-dependent I - V Characteristics at 2 K.

Figure S2 presents the I - V characteristics of Sample 1 at 2K under magnetic fields ranging from -200 Oe to 200 Oe. Solid lines indicate current sweeps from negative to positive, while dashed lines represent sweeps in the reverse direction. The critical current I_c reaches its maximum at zero magnetic field. Importantly, the retrapping current I_r remains nearly constant across all curves, suggesting that Joule heating has a negligible effect in this study.

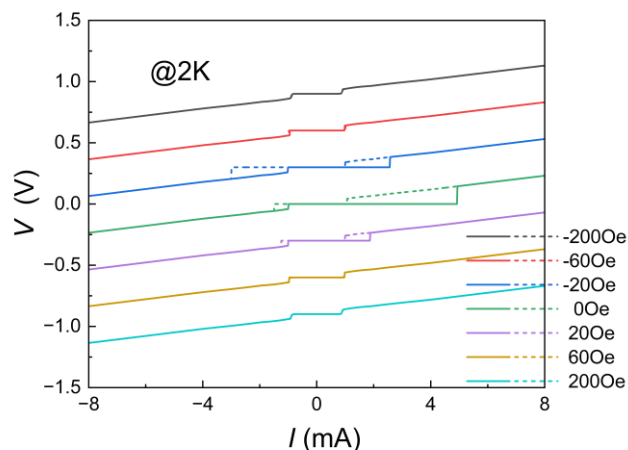


Figure S2. I - V characteristics of Sample 1 at 2 K under magnetic fields from -200 Oe to 200 Oe. Solid lines denote current sweeps from negative to positive, while dashed lines indicate sweeps in the reverse direction.

Supplementary Note S3. Magnetization-dependent ΔI_c behavior.

Figure S3 shows the dependence of ΔI_c on the applied magnetic field after reversing the magnetization direction of the Co layer. Prior to measurement, an oscillating demagnetization process was performed under a 1 T field, followed by a +1 T or -1 T field to ensure full saturation of the ferromagnetic layer in the desired direction. As shown, ΔI_c exhibits the expected odd-symmetric reversal upon magnetization switching^[3,4], highlighting the crucial role of the stray magnetic field in the SDE observed in this system.

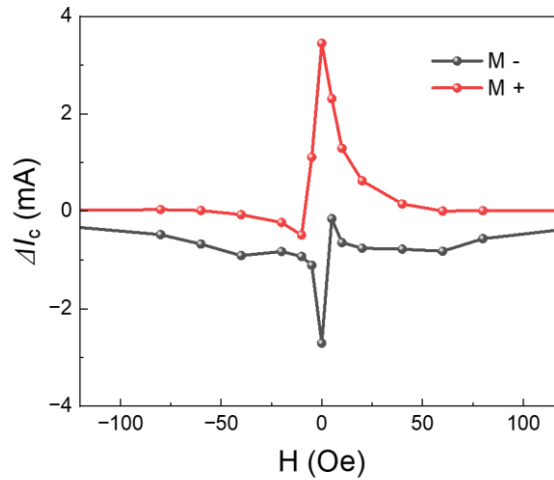


Figure S3. ΔI_c -H curves at 2K after magnetic saturation following oscillating demagnetization. The red curve corresponds to the Co layer magnetized along the +z direction, while the black curve represents magnetization along the -z direction.

- [1] W. B. Zeper, H. W. van Kesteren, B. A. J. Jacobs, J. H. M. Spruit, P. F. Carcia, *Journal of Applied Physics* **1991**, *70*, 2264.
- [2] P. F. Carcia, *Journal of Applied Physics* **1988**, *63*, 5066.
- [3] J. Xiong, J. Xie, B. Cheng, Y. Dai, X. Cui, L. Wang, Z. Liu, J. Zhou, N. Wang, X. Xu, X. Chen, S.-W. Cheong, S.-J. Liang, F. Miao, *Nat Commun* **2024**, *15*, 4953.
- [4] K.-R. Jeon, J.-K. Kim, J. Yoon, J.-C. Jeon, H. Han, A. Cottet, T. Kontos, S. S. P. Parkin, *Nat. Mater.* **2022**, *21*, 1008.